AIP Advances

Temperature-dependent properties of magnetic $CuFeS_2$ from first-principles calculations: Structure, mechanics, and thermodynamics

Cite as: AIP Advances **9**, 065021 (2019); https://doi.org/10.1063/1.5084308
Submitted: 06 December 2018 . Accepted: 17 June 2019 . Published Online: 25 June 2019

Rasoul Khaledialidusti, Abhishek Kumar Mishra, and Afrooz Barnoush

Temperature-dependent properties of magnetic $CuFeS_2$ from first-principles calculations: Structure, mechanics, and thermodynamics

Cite as: AIP Advances 9, 065021 (2019); doi: 10.1063/1.5084308
Submitted: 6 December 2018 • Accepted: 17 June 2019 •
Published Online: 25 June 2019

Rasoul Khaledialidusti,[1,a] Abhishek Kumar Mishra,[2] and Afrooz Barnoush[1]

AFFILIATIONS

[1] Department of Mechanical and Industrial Engineering, NTNU, Trondheim 7491, Norway
[2] Department of Physics, School of Engineering, University of Petroleum and Energy Studies, Dehradun 248007, India

[a] E-mail: rasoul.khaledialidusti@ntnu.no

ABSTRACT

Chalcopyrite ($CuFeS_2$) is an antiferromagnetic semiconductor with promising magnetic and electrical properties, although these properties are not yet completely understood. The structural, magnetic, and electronic properties of bulk $CuFeS_2$ were studied via first-principles plane-wave pseudopotential calculations based on density functional theory (DFT) using DFT+U and hybrid functional B3LYP methodology. The temperature-dependent structural, thermal, and mechanical properties of tetragonal $CuFeS_2$ were also investigated via density functional perturbation theory. Furthermore, the structural parameters, elastic constants, bulk and shear moduli, volume expansion, and specific heats as a function of temperature were evaluated. Tetragonal $CuFeS_2$ was found to exhibit negative thermal expansion behavior at temperatures lower than 100 K. A comprehensive comparison of the various calculated parameters with earlier published studies is also presented along with available experimental data and used as a basis to critically discuss the various properties of $CuFeS_2$.

I. INTRODUCTION

Chalcopyrite ($CuFeS_2$) is the main commercial source of copper and accounts for the majority of copper reserves worldwide.[1] Owing to its electrical, structural, and, in particular, band gap properties, $CuFeS_2$ is considered an interesting compound with numerous semiconductor applications, such as in optical devices,[2] photodiodes,[3] spintronic devices,[4] and thin-film intermediate-band solar cells.[5]

$CuFeS_2$, an antiferromagnetic semiconductor, crystallizes in a tetrahedral structure with space group $I\bar{4}2d$ (D_{2d}^{12}).[6] The magnetic and electrical properties of $CuFeS_2$ have not yet been completely elucidated and a detailed understanding of its complex antiferromagnetic behavior, including its structure, bonding, and magnetic and electronic properties, would be of immense value. Three different experimental measurements of the magnetic moment per Fe ion oriented along the crystallographic c axis, namely, 3.85, 3.42, and 3.88 μ_B, have been reported in three different works.[7–9] Similarly, a diverse range of values have been reported for the electronic band gap, including approximately 0.5 eV,[10–13] 2.6 eV from conductivity measurements using the four-point method,[14] and approximately 0.33–0.6 eV from recent infrared absorption measurements, which all reveal the semiconducting behavior of this material.[15] The electrical conductivity, Seebeck coefficient, and thermal conductivity of $CuFeS_2$ were recently calculated using first-principles calculations[16,17] and it was found that the electronic structure of $CuFeS_2$ governs the behavior of the Seebeck coefficient of this material. The lattice constants were measured via X-ray diffraction experiments as $a = b = 5.289$[18] (5.286)[19] Å and $c = 10.423$[18] (10.410)[19] Å. These properties are summarized in Table I. Computationally, $CuFeS_2$ is difficult to model using density functional theory (DFT) with simple local or semilocal functionals such as the local density approximation (LDA) and generalized gradient approximation (GGA), which are not reliable approximations for studying the properties of $CuFeS_2$.[20–24] It is apparent that the properties of $CuFeS_2$ are sensitive to the correct treatment of on-site electronic interactions, and neither LDA nor GGA are able to provide accurate treatment. The basis of this failure is insufficient description of the

TABLE I. Lattice parameters (a, c, and c/a), Cu–S and Fe–S distances (d_{Cu-S} and d_{Fe-S}), band gaps (E_g), and magnetic moments (m_s) for bulk $CuFeS_2$: Results of previous studies.

	a (Å)	c (Å)	c/a	d_{Cu-S} (Å)	d_{Fe-S} (Å)	E_g (eV)	m_s (μ_B)	Reference
Experiment and theory (Xα method)	5.289	10.423	1.971	2.302	2.257	- - -	- - -	Hall & Stewart[18] (X-ray diffraction)
	5.286	10.410	1.969	2.299	2.256	- - -	- - -	Kratz & Fuess[19] (X-ray diffraction)
	- - -	- - -	- - -	- - -	- - -	- - -	3.85[a]	[a]Donnay *et al.*[7] (neutron diffraction)
							3.42[b]	[b]Woolley *et al.*[8]
							3.88[c]	[c]Hamajima *et al.*[9] (Xα method)
	- - -	- - -	- - -	- - -	- - -	0.50[a]	- - -	[a]Goodman & Douglas;[10] [a]Austin *et al.*;[12] [a]Boltaks & Tarnovski;[11] [a]Pearce *et al.*[13]
						2.60[b]		[b]Teranishi[14]
						0.33–0.60[c]		[c]Engin *et al.*[15]
Computation	5.265	10.534	2.001	2.305	2.256	- - -	3.17	Łażewski *et al.*[21] (GGA-PW91)
	4.955	9.851	1.988	- - -	- - -	- - -	- - -	Zhou *et al.*[22] (LDA)
	5.08	10.003	1.969	- - -	- - -	- - -	- - -	Zhou *et al.*[22] (GGA-PBE)
	5.141	10.031	1.951	- - -	- - -	- - -	- - -	Zhou *et al.*[22] (LDA+U; U_{eff} = 3 eV)
	5.315	10.424	1.961	- - -	- - -	0.55	3.64	Zhou *et al.*[22] (GGA+U; U_{eff} = 3 eV)
	5.452[b]	10.710[b]	1.964[b]	2.395[b]	2.301[b]	1.82[a,b]	3.8[a]	[a]Conejeros *et al.*[23] (B3LYP & PBE+U; U_{eff} = 4.3 eV)
							3.93[b]	[b]Martínez-Casado *et al.*[24] (B3LYP)
						0.1		de Oliveira & Duarte[25] (GGA-PW91)

strong Coulomb repulsion between 3d electrons localized on ions.[20] Generally, DFT leads to underestimation of the band gap values of semiconductors compared to values determined using electron spectroscopy.[21,25] From earlier computational studies,[22,23] it was found that the DFT+U[25] methodology using the optimal effective Hubbard U characterizes the on-site Coulomb repulsion between 3d electrons by incorporating an additional energetic penalty for delocalization and hence provides a reasonably precise description of the measured electron energy loss spectra, lattice constants, cohesive energies, and elastic moduli. Furthermore, it was found that hybrid-exchange density functionals, such as Lee–Yang–Parr (B3LYP),[27,28] afford a more accurate description of the properties of $CuFeS_2$. Recently, the structural properties, band gap values, and magnetic properties of $CuFeS_2$ were studied using the B3LYP functional and the results displayed good agreement with experiments;[23,24] however, employing hybrid functionals is very computationally demanding and infeasible for studying larger systems such as surfaces. The results of the previous works are summarized in Table I.

In the present work, the hybrid-exchange B3LYP functional and DFT+U methodology were employed with the aim of studying the crystal structure and electrical and magnetic properties of $CuFeS_2$. In previous works,[22,23] different Hubbard correction terms of 3.0 and 4.3 eV were determined; however, all of the properties of $CuFeS_2$ (lattice constants, band gap value, and magnetic moment) were not simultaneously taken into account while determining the optimal U value. In addition, the obtained properties of $CuFeS_2$ were based on calculations for a single unit cell (1×1×1), although it was concluded that a 2×2×1 supercell might lead to more accurate atomic interactions in all directions.[21] In the current study, the DFT+U methodology was employed to attain a deeper understanding of the structural and electrical properties of $CuFeS_2$ by considering different properties simultaneously to determine the optimal Hubbard correction term. The analysis was performed for both 1×1×1 and 2×2×1 supercells to examine the influence of the supercell size on the selection of the optimal U value. The present study aims to clarify the ambiguity regarding the U value that exists in the literature, and we additionally report the structural parameters, elastic constants, bulk and shear moduli, volume expansion, and specific heats as a function of temperature. This work provides an important foundation for future studies involving the prediction and elucidation of the mechanical strength, stability, and phase transitions of $CuFeS_2$.

II. METHODOLOGY

Spin-polarized periodic DFT calculations were performed using the Vienna Ab initio Simulation Package (VASP) with a plane-wave basis set.[29–32] Electronic exchange and correlation were approximated using the hybrid-exchange B3LYP[27,28] functional for only a single unit cell (1×1×1) containing 16 atoms, because this has been demonstrated as a reliable functional to describe the geometry, energetics, and electronic properties of bulk $CuFeS_2$.[23,24]

To investigate the influence of the supercell size on the structural, electronic, and magnetic properties, a 2×2×1 supercell containing 64 atoms was also considered, which in principle should more accurately approximate the atomic interactions in all directions. The DFT+U[26] methodology with the formalism of Dudarev

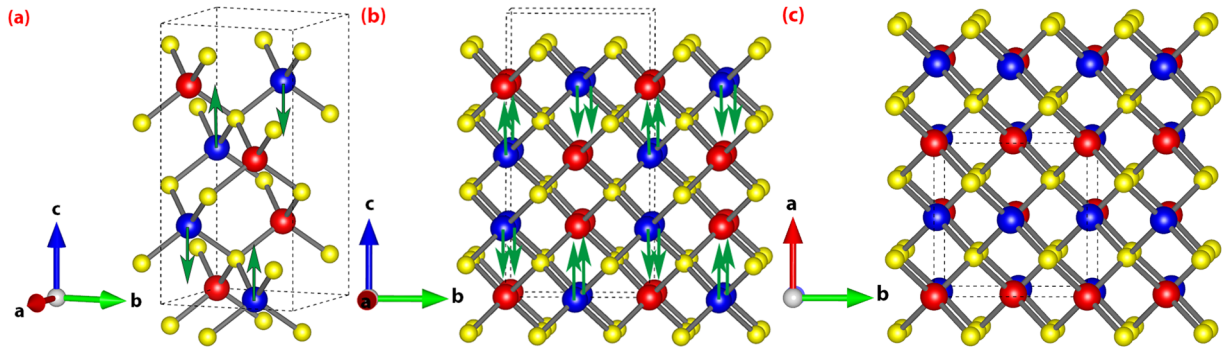

FIG. 1. Schematic depictions of the $CuFeS_2$ bulk structure: (a) a 1×1×1 supercell, (b) side view of a 2×2×1 supercell, and (c) top view of a 2×2×1 supercell. The red, blue, and yellow spheres represent the Cu, Fe, and S atoms, respectively. The S atoms are repeated at the edges owing to the periodic boundary conditions.

et al.[27] was applied for both supercells to capture the strong correlation effect of 3d electrons that is required for a more accurate description of the transition metals Cu and Fe. To obtain a set of energies for the magnetic states similar to that calculated using the hybrid-exchange B3LYP functional, a Hubbard correction term (i.e., the U_{eff} value)[26] was selected for the localized 3d electrons of Cu and Fe, where $U_{eff} = U - J$ is the difference between the Coulomb U and exchange J parameters. The GGA using the Perdew–Burke–Ernzerhof (PBE) functional[33,34] was applied for the exchange correlation in all calculations. Calculations including a Hubbard term for the Fe atoms were performed with various U_{eff} values in intervals of 1 eV up to 9 eV with a constant Hubbard term for the Cu atoms. Calculations with different Hubbard terms for the Cu atoms with U_{eff} values up to 6 eV were also performed; however, no significant changes were observed in either the resulting relative energies of the considered states or the atomic populations.

A conjugate gradient scheme was applied with iterative relaxation of the atomic positions with residual forces acting on the atoms of 0.01 eV/Å and a total energy convergence of 10^{-6} eV per unit cell. A very small Fermi smearing of 0.01 was employed for this semiconductor (i.e., $CuFeS_2$), because extrapolation of the total energy to absolute zero is only valid for metals with a continuous density of states (DOS) at the Fermi level.[35]

To find an accurate match of the calculated bulk and electronic structures as well as the magnetic properties with the experiments, the unit-cell geometry was first created using the Atomic Simulation Environment,[36] as depicted in Fig. 1. The atomic structures were also visualized using VESTA.[37]

Next, different plane-wave cutoff energies and k-point grids were examined to achieve a total energy convergence of 1 meV. Based on the obtained results, the energy convergence criterion was fulfilled with an energy cutoff of 550 eV and a 4×4×2 Monkhorst–Pack[31] k-point mesh for the Brillouin zone sampling of the 1×1×1 supercell of $CuFeS_2$. This plane-wave cutoff was kept constant throughout the calculations; however, the number of k points was varied with the unit-cell size. The Brillouin zone of the 2×2×1 supercell was sampled using a 4×4×4 Monkhorst–Pack[31] k-point mesh. The electronic DOSs were calculated by employing relatively dense 8×8×4 and 8×8×8 Monkhorst–Pack[31] k-point meshes for the 1×1×1 and 2×2×1 supercells, respectively.

The thermal properties and temperature-dependent lattice constants of $CuFeS_2$ were studied via first-principles phonon calculations performed using density functional perturbation theory.[38,39] The phonon dispersions were calculated using the PHONOPY code[40,41] within the 2×2×1 supercell with a 4×4×4 Monkhorst–Pack[31] k-point mesh. We also employed the quasi-harmonic approximation (QHA)[42] to calculate the temperature-dependent properties of $CuFeS_2$. For the calculation of phonon properties, the energy convergence criterion was set to 10^{-8} eV to ensure sufficient accuracy of the generated force constants. The Helmholtz free energy F for a given temperature and volume was computed using $F(T,V) = E_{DFT}(V) + F_{vib}(T,V)$, where $E_{DFT}(V)$ is the DFT total energy and $F_{vib}(T,V)$ is the vibrational free energy. The full details were reported by Togo *et al.*[40–42]

III. RESULTS AND DISCUSSION

A. Crystal structure and properties

$CuFeS_2$ possesses a tetrahedral structure with a unit cell of $I\bar{4}2d$ symmetry containing 16 atoms (four Cu, four Fe, and eight S), whereas a 2×2×1 supercell consists of 64 atoms (16 Cu, 16 Fe, and 32 S). The optimized structures of the unit cell and 2×2×1 supercell are depicted in Fig. 1. The properties of $CuFeS_2$ were calculated for the antiferromagnetic (AFM) structure phase, which was found to be the most stable (lowest energy) magnetic solution for this system[23] and is in reasonable agreement with experiments,[7,8] where $CuFeS_2$ was antiferromagnetic with the magnetic moments of the Fe centers directed along the c axis. In this lowest-energy AFM state, the spin directions of the Fe atoms alternate between each layer perpendicular to the crystallographic c axis, as shown in Fig. 1.

The DFT calculation results of the lattice parameters, magnetic moments (m_s), and band gap values (E_g) for both cells are listed in Tables II and III. The results of previous theoretical and experimental studies are summarized in Table I.

From the previous computational studies performed (Table I), as mentioned in Sec. I, the LDA and GGA functionals were found not to be reliable approximations for studying the various properties of $CuFeS_2$. Comparison of the experimentally measured lattice parameters with the values obtained from the previous

TABLE II. Lattice parameters (*a*, *c*, and *c*/*a*), Cu–S and Fe–S distances (d_{Cu-S} and d_{Fe-S}), band gaps (E_g), and magnetic moments (m_s) for the 1×1×1 supercell of bulk $CuFeS_2$: Comparing the quantities calculated using DFT+*U* with different U_{eff} values and B3LYP.

U_{eff}	*a* (Å)	*c* (Å)	*c*/*a*	d_{Cu-S} (Å)	d_{Fe-S} (Å)	E_g (eV)	m_s (μ_B)
0	5.285	10.422	1.972	2.310	2.247	- - -	3.07
1	5.285	10.421	1.972	2.300	2.256	0.16	3.29
2	5.286	10.418	1.971	2.293	2.262	0.43	3.46
3	5.286	10.419	1.971	2.284	2.272	0.62	3.59
4	5.286	10.418	1.971	2.279	2.277	0.69	3.70
5	5.286	10.418	1.971	2.275	2.280	0.75	3.80
6	5.297	10.374	1.959	2.271	2.285	0.74	3.89
7	5.266	10.497	1.993	2.270	2.286	0.78	3.98
8	5.275	10.532	2.003	2.270	2.285	0.78	4.08
9	5.256	10.538	2.005	2.270	2.286	0.84	4.19
B3LYP	5.287	10.414	1.970	2.305	2.252	1.85	3.8

studies employing these exchange-correlation functionals also reveals this unsuitability of these functionals, although the GGA functionals PBE (in the work of Zhou *et al.*[22]) and PW91 (in the work of Łażewski *et al.*[21]) afforded more reliable results compared to the LDA functional (in the work of Zhou *et al.*[22]). Furthermore, in the work of Łażewski *et al.*,[21] even a 2×2×1 supercell (using PW91) could not accurately describe the structure of $CuFeS_2$, although it was closer to the experimental findings than the results of Zhou *et al.*[22] performed using a 1×1×1 supercell (using PBE). However, the results of Zhou *et al.* demonstrate that employing the DFT+*U* methodology using the GGA functional PBE for a 1×1×1 supercell with U_{eff} = 3 eV could provide a significant improvement with respect to the estimated lattice constants.[22] Surprisingly, the results of Martínez-Casado *et al.* demonstrated greater deviation from the experimental findings when using the hybrid-exchange B3LYP functional.[24]

In the current study, a greater improvement in the optimized lattice parameters was observed upon employing the hybrid-exchange B3LYP functional or DFT+*U* methodology using the PBE functional compared to the previous theoretical studies. No significant changes in the lattice parameters were identified for U_{eff} values less than 6 eV; however, the obtained results started to deviate from the experimental values for U_{eff} values greater than 6 eV (Tables II and III). Our results for U_{eff} = 3 eV were found to be more consistent with the experimental values compared to the work of Zhou *et al.*[22] using the same U_{eff} and exchange-correlation functional values. This improvement may be attributable to the fact that we employed a denser *k*-point mesh of 4×4×8 and a higher energy cutoff of 550 eV compared to the 3×3×4 *k*-point mesh and energy cutoff of 440 eV used in the work of Zhou *et al.*,[22] which were insufficient to accurately represent the electronic structure. In the present study, we did not observe any significant differences between the optimized lattice parameters of the 1×1×1 and 2×2×1 supercells, mainly for U_{eff} values less than 6 eV (Tables II and III).

TABLE III. Lattice parameters (*a*, *c*, and *c*/*a*), Cu–S and Fe–S distances (d_{Cu-S} and d_{Fe-S}), band gaps (E_g), and magnetic moments (m_s) for the 2×2×1 supercell of bulk $CuFeS_2$: Comparing the quantities calculated using DFT+*U* with different U_{eff} values.

U_{eff}	*a* (Å)	*c* (Å)	*c*/*a*	d_{Cu-S} (Å)	d_{Fe-S} (Å)	E_g (eV)	m_s (μ_B)
0	5.285	10.423	1.972	2.310	2.246	- - -	3.07
1	5.285	10.422	1.972	2.299	2.257	0.14	3.30
2	5.285	10.421	1.972	2.291	2.265	0.43	3.46
3	5.285	10.421	1.972	2.285	2.271	0.61	3.59
4	5.285	10.421	1.972	2.279	2.277	0.69	3.70
5	5.286	10.419	1.971	2.275	2.280	0.75	3.80
6	5.290	10.402	1.966	2.272	2.284	0.73	3.88
7	5.278	10.449	1.980	2.270	2.285	0.76	3.98
8	5.261	10.518	1.999	2.270	2.286	0.76	4.08
9	5.256	10.539	2.005	2.271	2.285	0.83	4.19

B. Magnetic properties

To evaluate the magnetic properties of $CuFeS_2$, as stated in Sec. I, the different magnetic states of the supercells, namely, the AFM and ferromagnetic (FM) phases, were first analyzed, and the AFM configuration was found to be the lowest-energy (ground) state. Next, the spin configurations corresponding to the AFM phases were initially assigned to the Fe atoms (as the most stable spin arrangement) in the conventional supercells, as depicted in Fig. 1. As can be seen, the directions of the spins of the Fe atoms alternated between each layer perpendicular to the crystallographic *c* direction. This magnetic configuration is in excellent agreement with experiments[7,8] and previously published computational studies,[21,24] where $CuFeS_2$ was predicted to be antiferromagnetic with the magnetic moments of the Fe centers directed along the *c* axis.

Experimentally, there exists a discrepancy in the reported literature regarding the value of the effective magnetic moment for the Fe atoms. Donnay *et al.* reported a value of 3.85 μ_B based on neutron diffraction measurements of natural mineral samples (Experiment A),[7] whereas Wooley *et al.* disclosed a value of 3.42 μ_B for the synthetic material (Experiment B).[8] In addition, Hamajima *et al.* calculated a value of 3.88 μ_B using the Xα method (Experiment C).[9] These experimentally measured values are listed in Table I and indicated by horizontal dashed lines in Fig. 2. Similarly, previously published computational studies evaluating the magnetic properties of the AFM ground state of $CuFeS_2$ have reported different values of the spin density ranging from 3.17 to 3.93 μ_B.[21,24] Łażewski *et al.* reported an Fe spin moment of 3.17 μ_B based on pure DFT using the GGA functional PW91.[21] Although this value is similar to the range of magnetic moments observed experimentally (i.e., 3.42–3.88),[7–9] it is known that pure DFT provides an incorrect description of $CuFeS_2$ owing to the nonzero self-interaction errors of DFT and the delocalization of electrons in this material. Zhou *et al.* reported an Fe spin moment of 3.64 μ_B based on DFT+*U* using the GGA functional PBE with a U_{eff} value of 3 eV,[22] which is closer to the experimental values.[7–9] Values of 3.8 and 3.93 μ_B were obtained from DFT-B3LYP calculations by Conejeros *et al.*[23] and Martínez-Casado *et al.*,[24] respectively. Conejeros *et al.* also calculated the same value of 3.8 μ_B based on DFT+*U* using the GGA functional PBE with a U_{eff} value of 4.3 eV.[23]

The results of the present study are in accordance with both previous experimental and computational studies. DFT-B3LYP

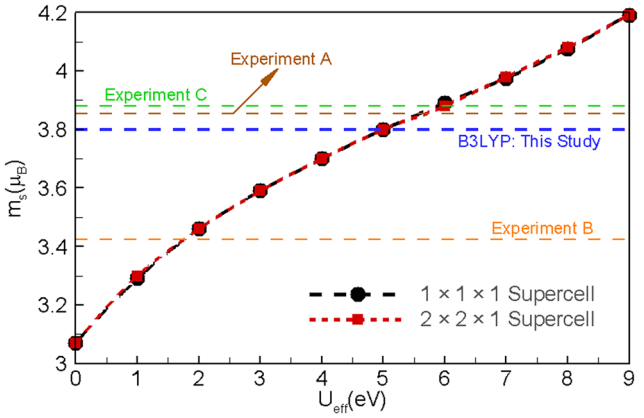

FIG. 2. Magnetic moment (m_s) of the Fe atoms as a function of U_{eff}. Experimental values from previous works and the value calculated using B3LYP in this study are indicated by horizontal dashed lines.

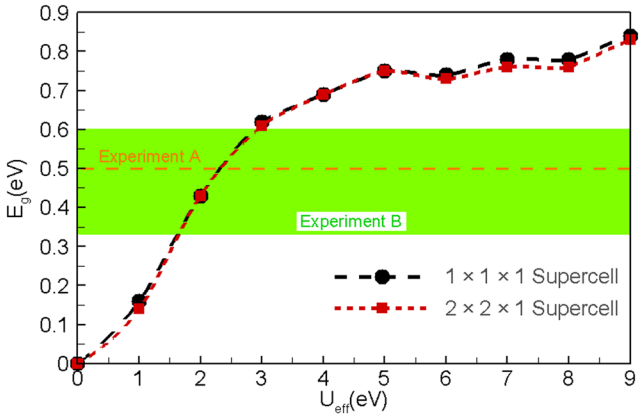

FIG. 3. Variation of the band gap (E_g) of $CuFeS_2$ as a function of U_{eff}. The horizontal dashed lines and green region indicate the range of experimental values.

calculations afforded an Fe spin moment of 3.8 μ_B for both supercells (blue horizontal dashed line in Fig. 2), which is identical to the value obtained by Conejeros *et al.*[23] As the hybrid-exchange B3LYP functional is very computationally expensive for larger systems such as surfaces, we investigated whether the same value of the magnetic moment could be obtained using a reasonable external Hubbard U parameter. Consequently, various U_{eff} values for the Fe atoms in intervals of 1 eV up to 9 eV were applied with a constant Hubbard term for the Cu atoms. We did not observe any significant changes in either the resulting relative energies of the considered states or the atomic populations using different Hubbard terms for the Cu atoms.

Figure 2 shows the variation of the magnetic moment of the Fe atoms observed for different U_{eff} values, where an insignificant value of 0.005 μ_B was obtained for the Cu atoms. As can be seen, the difference between the results obtained for the 1×1×1 and 2×2×1 supercells was negligible. A magnetic moment of 3.59 μ_B for the Fe atoms was observed for U_{eff} = 3 eV, in contrast to the value of 3.64 μ_B reported by Zhou *et al.* using the same value of U_{eff} (see Tables I and II and Fig. 2).[22] This small difference may be attributable to the denser k-point grids and greater plane-wave cutoff energy applied in the present study. We obtained the same value as that calculated using DFT-B3LYP by adopting U_{eff} = 5 eV; however, a U_{eff} value of 4.3 eV was applied by Conejeros *et al.* to obtain the same result.[23] We repeated our calculations with this U_{eff} value, but no significant changes were observed in any of the parameters compared to the U_{eff} value of 4 eV (see Tables I and II and Fig. 2).

C. Electronic band structure

The electronic band structure was calculated after performing high-accuracy self-consistent electronic calculations to optimize the structures with 4×4×2 and 2×2×2 k-point grids for the 1×1×1 and 2×2×1 supercells, respectively. To calculate the electronic band structure with high accuracy, self-consistent field calculations were performed using denser k-point grids of 16×16×8 and 8×8×8 for the 1×1×1 and 2×2×1 supercells, respectively. The band gap values calculated using different U_{eff} values are plotted in Fig. 3. The results revealed almost the same band gap for both the 1×1×1 and 2×2×1 supercells and a very small deviation was observed for U_{eff} values exceeding 5 eV. This deviation may be attributable to the different lattice constants obtained for the two supercells (see Tables II and III).

As can be seen from Fig. 3, no band gap was observed at U_{eff} = 0 eV and the band gap of the system opened upon increasing the U_{eff} value with a shift of the d states beyond the Fermi energy (see Fig. 4). Both the band gap (E_g) and magnetic moment (m_s) increased with increasing U_{eff} (Figs. 2 and 3). The DFT-calculated electronic DOS and partial densities of states (PDOSs) for the Cu, Fe, and S atoms of the optimized ground state of $CuFeS_2$ are presented in Fig. 4. As can be seen, Fe orbitals generally occupied the conduction band, whereas the valence band was mostly dominated by Cu orbitals.

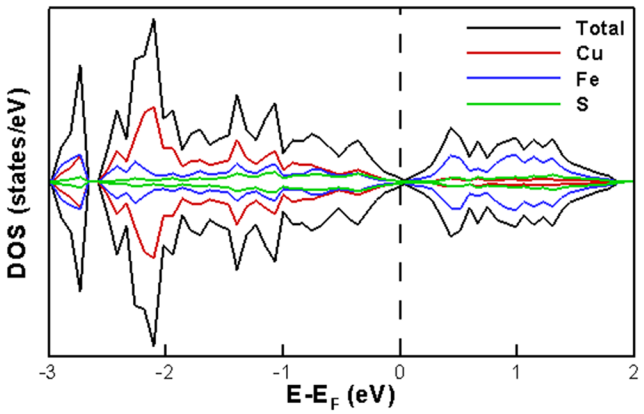

FIG. 4. Density of states (DOS) of $CuFeS_2$ calculated via DFT. The total DOS is indicated by the black line and the partial densities of states (PDOSs) for the Cu, Fe, and S atoms are indicated by the red, blue, and green lines, respectively.

The reported experimental values of the band gap do not provide a clear consensus, making the band gap a poorly understood property of $CuFeS_2$; however, all of the previous experimental works predicted $CuFeS_2$ to be a semiconductor. Although a value of 0.5 eV was measured for the band gap of $CuFeS_2$ (Experiment A),[7–9] as indicated by the horizontal dashed line in Fig. 3, Teranishi *et al.* reported a value of 2.6 eV.[14] Recently, values ranging between 0.33 and 0.6 eV were reported by Engin *et al.* (Experiment B),[15] as indicated by the green region in Fig. 3. Previously published computational studies evaluating the electrical properties of the AFM ground state of $CuFeS_2$ have also identified different values for the band gap.[21–25] It is known that the B3LYP functional is generally more reliable for estimating the electronic band gap than pure DFT using LDA or GGA functionals, which tend to underestimate the band gap.[23,24] Edelbro *et al.* predicted $CuFeS_2$ to be conducting on the basis of LDA calculations,[43] whereas GGA-PW91 calculations performed by de Oliveira and Duarte[25] indicated that $CuFeS_2$ is a semiconductor with an indirect band gap of 0.1 eV. Zhou *et al.* predicted a larger value of 0.55 eV for the band gap using DFT+U with U_{eff} = 3 eV.[22] Furthermore, a band gap of 1.82 eV was predicted using the B3LYP functional by Conejeros *et al.*[23] and Martínez-Casado *et al.*,[24] which is inconsistent with the previous computational studies using

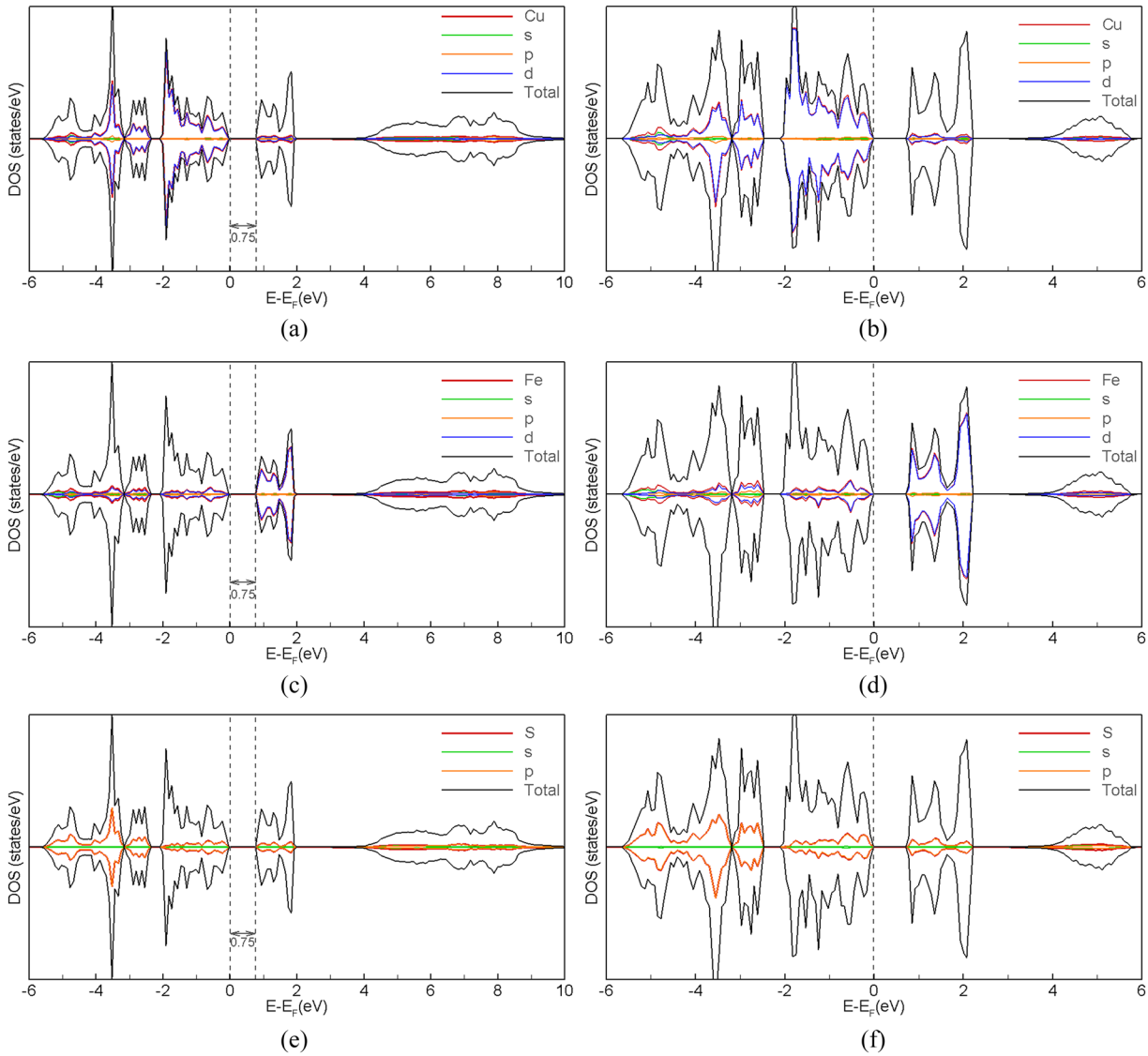

FIG. 5. Densities of states (DOSs) of $CuFeS_2$ calculated via DFT+U (U_{eff} = 5 eV) (left) and B3LYP (right). The total DOS is indicated by the black line, and the partial densities of states (PDOSs) for the Cu, Fe, and S atoms are indicated by the red lines. The projected DOSs over the d orbitals, p orbitals, and s orbitals are indicated by the blue, orange, and green lines, respectively.

different treatments for electronic exchange and correlation. In the present study, the calculated band gap value was 1.80 eV using the B3LYP functional, which is in excellent agreement with the previous studies that applied the same electronic exchange and correlation functions.

The results of the present study show that the lattice parameters (Tables I and II), m_s (Fig. 2), and E_g (Fig. 3) increased with increasing U_{eff}, and increasing the value of U_{eff} beyond 5 eV caused these properties to start deviating from the experimental values. As mentioned above, in the present study, applying a U_{eff} of 5 eV led to a predicted magnetic state similar to that calculated using the hybrid B3LYP functional; however, the band gap predicted with this U_{eff} value was 0.75 eV, which is less than the value of 1.8 eV predicted using B3LYP. The calculated DOSs and PDOSs for the Cu, Fe, and S atoms of the optimized ground state of $CuFeS_2$ for these two electronic exchange and correlation functions are plotted in Fig. 5. The general trend for the various orbitals was the same for B3LYP and DFT+U, despite the different band gaps, and in agreement with the computational study by Conejeros *et al.*[23] A more detailed analysis of the PDOSs revealed that the contributions of the Cu(4s), Fe(4s), and S(3s) orbitals were insignificant in the vicinity of the Fermi level for both B3LYP and DFT+U. It can be clearly observed that the conduction band was mainly dominated by the Fe(3d) orbitals, whereas the valence band was mostly composed of the Cu(3d) orbitals for both B3LYP and DFT+U.

D. Thermodynamic properties

Phonon properties typically vary with changing volume because the crystal potential is an anharmonic function of volume.[41] In this study, the thermal properties were calculated under the framework of the QHA, which takes into account this anharmonic volume dependence of phonon properties during the calculation of thermodynamic properties. However, the harmonic approximation is simply applied at each volume, with a pressure value of zero and a Gibbs energy equal to the Helmholtz free energy.

As stated in Sec. II, in the QHA, the Helmholtz free energy $F(V,T)$ is calculated using $F(V,T) = E(V) + F_{vib}(V,T)$, where $E(V)$ is the static energy from DFT calculations and $F_{vib}(V,T)$ is the vibrational free energy, which is obtained using $F_{vib}(V,T) = k_B T \sum \log\left\{2\sinh\left(\frac{\hbar\omega_v(q,V)}{2k_B T}\right)\right\}$, where $\omega_v(q,V)$ is the phonon frequency at a fixed volume V and a given vector q.

In this study, the total Helmholtz free energy was calculated for several volumes (from 97%V to 103%V) around the equilibrium volume to comprehensively investigate the influence of temperature on the volume. The magnetic transition from AFM to FM was evaluated for these volumes and the results of the ground-state energy confirmed that this transition did not occur when the equilibrium volume was compressed to 97%V or expanded to 103%V. The total Helmholtz free energy was calculated for these volumes over the same temperature ranges (from 0 to 300 K) and temperature steps (10 K). After calculating the free energies, they were fitted using the Birch–Murnaghan equation.[44,45] The optimal volume at each temperature was determined on the basis of the minimum Helmholtz free energy. The optimal geometry fitted using the Birch–Murnaghan equation[44,45] would theoretically afford very precise estimates of the lattice parameters. Finally, the thermal expansion properties were obtained using PHONOPY code under the QHA.

Within the framework of the QHA, the theoretical calculations may accurately capture the experimental results at low temperatures if the structure is stable; however, the influence of anharmonic terms increases with increasing temperature. At higher temperatures, the calculated results may start to deviate from the experimental measurements despite being qualitatively consistent. Therefore, the quartic anharmonic terms should be taken into consideration to more accurately study the thermal behavior of any structure at temperatures exceeding 300 K.

E. Negative thermal expansion behavior

The calculated Helmholtz free energy as functions of volume and temperature is plotted in Fig. 6(a), in which each blue line fitted using the Birch–Murnaghan equation corresponds to a particular temperature. The minimum Helmholtz free energies, indicated by red circles, correspond to the optimal volumes from 0 to 300 K. The variation of the optimal volume with temperature is plotted in Fig. 6(b). The results clearly demonstrate the negative thermal expansion behavior of tetragonal $CuFeS_2$ at low temperatures, where

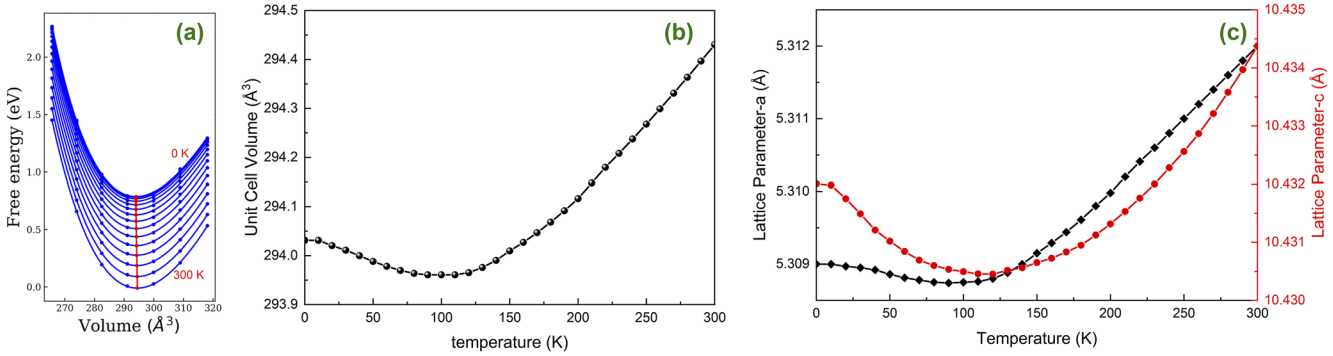

FIG. 6. Computed negative thermal expansion behavior of tetragonal $CuFeS_2$. (a) Helmholtz free energy as functions of volume and temperature (0 to 300 K in 20 K steps). The closed blue circles indicate the calculated values and the solid curves represent the fitting results. The closed red circles indicate the energy minima of the curves and the corresponding equilibrium volumes. (b) Temperature dependence of the unit-cell volume. (c) Temperature dependence of the lattice parameters *a* and *c*.

the unit-cell volume decreased continuously with increasing temperature from 0 K, such that the volume reached a minimum value at approximately 100 K. Positive thermal expansion behavior was observed at temperatures exceeding 100 K.

To calculate the lattice parameters at each temperature, it is necessary to minimize the Helmholtz free energy functions with the deformation strain (ζ) instead of volume. This is mainly required because volume is a multiple-variable function of the lattice parameters for low-symmetry crystals and it is infeasible to directly calculate the lattice parameters owing to the difficulty associated with minimizing multiple-variable functions. The details were explained by Shao *et al.*[46] In this study, the lattice parameter a (=b) was calculated by applying a (ζ, ζ, 0, 0, 0, 0) configuration tensor to the lattice vectors with ζ values between ±3% in increments of 0.5%. Next, the Helmholtz free energy was calculated for each value of ζ at various temperatures and minimized with respect to ζ to calculate the equilibrium deformation strain ζ_T^0. The lattice parameter a can be calculated using $a_T = \zeta_T^0 a_0$, where a_0 is the optimal lattice parameter at 0 K obtained via first-principles geometry optimization and a_T is the equilibrium lattice parameter at a given temperature. Finally, the lattice parameter c can be directly obtained from the relationship between the optimal volume (V_T) and a_T at a given temperature using $c_T = V_T/(a_T)^2$.

Figure 6(c) shows the variation of the equilibrium lattice parameters of $CuFeS_2$ with temperature. As can be seen, the optimal lattice parameters a and c were 5.309 Å and 10.432 Å, respectively, at 0 K. Both lattice parameters decreased to a minimum value with increasing temperature and then started to increase at higher temperatures. It is interesting to note that the two lattice parameters reached their corresponding minima at two significantly different temperatures, namely, approximately 90 and 125 K for lattice parameters a and c, respectively.

F. Heat capacity

PHONOPY code under the QHA was used to calculate the temperature dependence of the isobaric heat capacity $C_p(T)$ of $CuFeS_2$, as plotted in Fig. 7. The measured values of $C_p(T)$ reported by Robie *et al.* for synthetic samples at temperatures ranging from 6.3 to 303.5 K are also plotted for the purposes of comparison.[47] Comparison of these results revealed that the calculated values of C_p were in good agreement with the experimentally measured values at temperatures below 200 K, whereas the two sets of results gradually deviated at temperatures exceeding 200 K owing to the lattice anharmonicity at higher temperatures, as mentioned in Sec. III D.

G. Temperature-dependent elastic constants

The temperature dependence of the elastic constants of $CuFeS_2$ was calculated from the phonon DOS using the QHA, in which isothermal elastic constants can be considered as strain derivatives of the Helmholtz free energy using the following formula:

$$F[X(\zeta);T] = E[X(\zeta)] + F_{\text{vib}}[X(\zeta);T], \quad (1)$$

where $E[X(\zeta)]$ is the total energy of the specific deforming configuration and $F_{\text{vib}}[X(\zeta);T]$ is the vibrational Helmholtz free energy calculated from the phonon DOS using the QHA. The details were reported by Shao *et al.*[46] and Wen *et al.*[48]

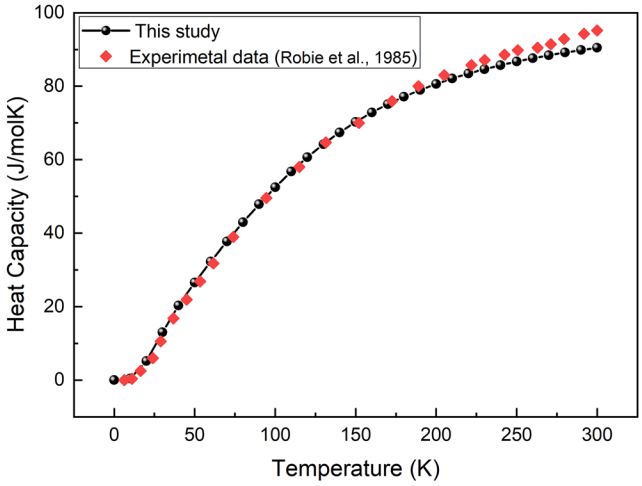

FIG. 7. Calculated temperature dependence of the isobaric heat capacity C_p compared with the experimental data reported by Robie *et al.*[44]

There are seven independent elastic constants, namely, c_{11}, c_{22}, c_{33}, c_{44}, c_{66}, c_{12}, and c_{13}, where $c_{11} = c_{22}$. To calculate the temperature-dependent elastic constants of tetragonal $CuFeS_2$, six sets of deformed crystals were constructed to obtain six sets of the Helmholtz free energy $F[X(\zeta);T]$ curves with respect to the strain ζ at a given temperature. We selected (ζ, −ζ, $\zeta^2/(1-\zeta^2)$, 0, 0, 0), (ζ, $\zeta^2/(1-\zeta^2)$, −ζ, 0, 0, 0), (ζ, ζ, 0, 0, 0, 0), (ζ, 0, ζ, 0, 0, 0), ($\zeta^2/(1-\zeta^2)$, 0, 0, 2ζ, 0, 0), and (0, 0, $\zeta^2/(1-\zeta^2)$, 0, 0, 2ζ) as the six deformation modes. It is worth noting that the Helmholtz free energy is only a function of strain ζ at a given temperature for fixed deformation modes; hence, the minimum of the Helmholtz free energy function with respect to variable ζ is the equilibrium Helmholtz free energy at that temperature. Next, the six Helmholtz free energy densities per unit-cell volume with respect to the normal strain ζ were calculated for temperatures ranging from 0 to 300 K in increments of 50 K. The corresponding second-order strain derivatives of the Helmholtz free energy per unit-cell volume were derived with

TABLE IV. Calculated elastic constants (c_{ij}, GPa), bulk modulus (B, GPa), and shear modulus (G, GPa) for tetragonal $CuFeS_2$ at 0 K and 0 GPa, alongside other theoretical results obtained under the same thermodynamic conditions and experimental data recorded at 10 and 300 K and 0 GPa.

	Computation at 0 K			Experiment[49]	
	Present study	Łażewski *et al.*[21]	Zhou *et al.*[22]	10 K	300 K
c_{11}	103.5	89.8	106.7	213.5	205.0
c_{33}	102.2	94.1	103.2	433.8	422.4
c_{44}	32.6	25.5	29.3	58.8	56.5
c_{66}	30.6	27.8	25.2	122.5	116.2
c_{12}	73.4	61.3	77.5	101.3	96.1
c_{13}	77.1	66.9	78	31.1	29.8
B	84.9	73.6	87.1	129.6	124.6
G	22.6	19.8	21.0	85.2	82.0

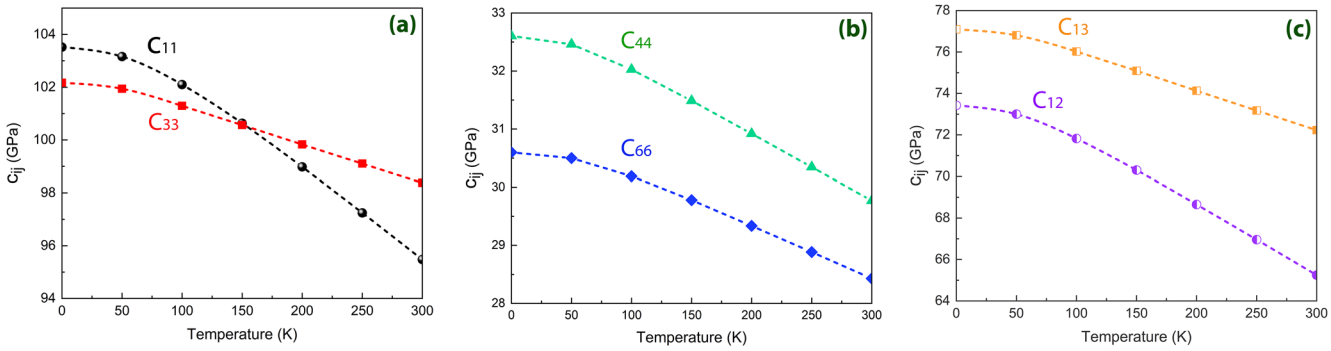

FIG. 8. Elastic constants of $CuFeS_2$ as a function of temperature: (a) c_{11} and c_{33}, (b) c_{44} and c_{66}, (c) c_{12} and c_{13}.

ζ values between ±3% in increments of 0.5% by polynomial fitting of these Helmholtz free energies (the corresponding curves are given as Fig. S1 in the supplementary material). Furthermore, the isothermal elastic constants were calculated by solving the following system of linear equations providing the correlation between the second-order strain derivatives and the linear combination of isothermal elastic constants:

$$\begin{cases} c_{11}^T + c_{22}^T - 2c_{12}^T = D_1^T \\ c_{11}^T + c_{33}^T - 2c_{13}^T = D_2^T \\ c_{11}^T + c_{22}^T + 2c_{12}^T = D_3^T \\ c_{11}^T + c_{33}^T + 2c_{13}^T = D_4^T \\ 4c_{44}^T = D_5^T \\ 4c_{66}^T = D_6^T \end{cases} \quad (2)$$

where $D_1^T \ldots D_i^T \ldots D_6^T$ are the second-order strain derivatives of the Helmholtz free energy under the six deformation modes, and $c_{11}^T \ldots c_{ij}^T \ldots c_{66}^T$ are the elastic constants at a given temperature and zero pressure. The energy of the unit cell is a function of both volume and deformation strain. In these calculations, volume-conserving deformations were applied to calculate the shear elastic constants c_{44} and c_{66}. This was expected to permit highly accurate calculation of the elastic constants because the energy of the deformed unit cell depends only on distortion and not volume. The calculated elastic constants (c_{ij}), bulk modulus (B), and shear modulus (G) of $CuFeS_2$ at 0 K and 0 GPa are presented in Table IV, alongside other theoretical results obtained under the same thermodynamic conditions[21,22] and experimental data recorded at 10 and 300 K and 0 GPa.[49] The elastic constants calculated in the present study are consistent with the previously reported theoretical results[21,22] and in better agreement with those reported by Zhou *et al.*, in which the DFT+U methodology using the GGA functional PBE was employed.[22] However, the calculated elastic constants were significantly lower than the experimental values.[51] It was concluded by Łażewski *et al.*[21] and Zhou *et al.*[22] that the very high values of the reported experimental elastic constants are unusual and may not adequately represent the pseudocubic elastic behavior of ternary compounds such as $CuFeS_2$.

The values of B and G were obtained from the calculated c_{ij} values using the Voigt–Reuss–Hill approximation.[50] A B value of 91±15 GPa was also reported in a pressure-dependent X-ray diffraction study of tetragonal $CuFeS_2$.[51] This only available experimental measurement of the bulk modulus is comparable with the values estimated from the elastic constants. B values of 73.6 and 87.1 GPa were estimated from the calculated elastic constants by Łażewski *et al.*[21] and Zhou *et al.*,[22] respectively, where the latter value is in closer agreement with the experimental value of 91±15 GPa. The B value of 84.9 GPa obtained in the present study is also in satisfactory agreement with the experimental value. The experimentally measured elastic constants yielded B values of 129.6 and 124.6 GPa at 10 and 300 K, respectively, which clearly deviate from the experimental value. G values of 19.8 and 21.0 GPa were estimated from the calculated elastic constants by Łażewski *et al.*[21] and Zhou *et al.*,[22] respectively, which are similar to the value of 22.6 GPa obtained in the present study.

As stated above, the phonon DOS using the QHA provides the ability to calculate the temperature dependence of the elastic constants. Plots showing the variation of all of the elastic constants of $CuFeS_2$ as a function of temperature are presented in Fig. 8. All of the elastic constants decreased with increasing temperature,

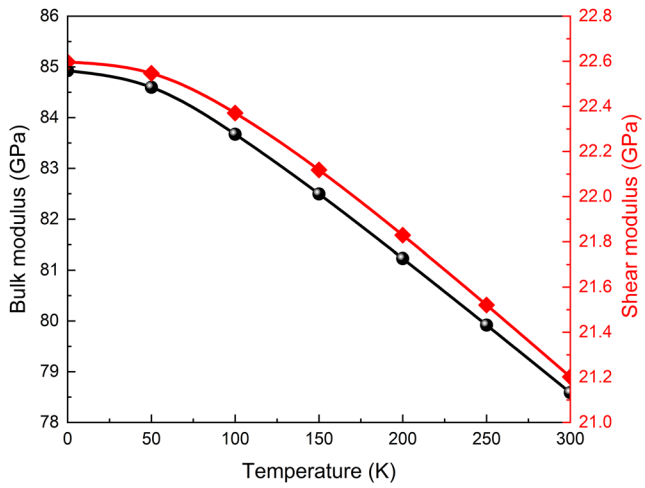

FIG. 9. Estimated bulk and shear moduli as a function of temperature.

although the rate of change varied. The results clearly revealed that c_{11} decreased relatively rapidly with increasing temperature from 103.5 GPa at 0 K to 95.5 GPa at 300 K, such that it was equal to c_{33} at 150 K and less than c_{33} at temperatures exceeding 150 K.

The temperature dependences of the bulk and shear moduli were also estimated from the calculated elastic constants, as plotted in Fig. 9. Both moduli decreased with increasing temperature, from 84.9 to 78.6 GPa for B and from 22.6 to 21.2 GPa for G as the temperature was increased from 0 to 300 K.

IV. CONCLUSIONS

We have applied different DFT-based methodologies to investigate the structural, magnetic, and electrical properties of tetragonal $CuFeS_2$. The structural properties, elastic constants, bulk and shear moduli, volume expansion, and specific heats as a function of temperature have been calculated. In addition to the hybrid B3LYP functional, the DFT+U methodology was employed with systematic variation of the U parameter for the Fe atoms in the range of 0–9 eV in 1 eV intervals and a constant Hubbard term for the Cu atoms to determine the structural parameters, magnetic moment, and band gap in improved agreement with experimental data. It was found that these properties were not significantly affected by variation of the Hubbard term for the Cu atoms. U_{eff} values of 1 to 5 afforded very good agreement with the experimentally obtained lattice parameters, while further increasing U_{eff} led to deviation from the experimental data. The most reasonable match with the experimental magnetic moment was obtained using U_{eff} values of 4 or 5 eV; moreover, the magnetic moment calculated using the hybrid B3LYP functional was found to be identical to that calculated using DFT+U with a U_{eff} value of 5 eV. The electronic structure and band gap of $CuFeS_2$ have not been accurately determined previously and a large difference was observed between the values calculated using the hybrid B3LYP and DFT+U methods. As the hybrid B3LYP functional is very computationally demanding and inappropriate for large systems such as surfaces, the results indicate that the DFT+U methodology with a U_{eff} value of 5 eV, which afforded the same magnetic moment as the hybrid B3LYP functional, is the most robust methodology for analyzing larger systems such as $CuFeS_2$.

The present work also provided the temperature-dependent elastic constants of $CuFeS_2$ by combining the quasi-static approximation to elasticity and the quasi-harmonic phonon approximation to volume expansion. Examination of the temperature-dependent properties of $CuFeS_2$ revealed the occurrence of negative thermal expansion behavior at temperatures lower than 100 K. This provides theoretical evidence to support the possible use of tetragonal $CuFeS_2$ as a new negative thermal expansion material that warrants further attention. The obtained elastic constants were in very good agreement with previous theoretical studies performed at 0 K. All of the calculated temperature-dependent elastic constants decreased with increasing temperature, although the rate of change varied, and c_{11} decreased relatively rapidly with increasing temperature such that it became equal to c_{33} at 150 K and less than c_{33} at temperatures exceeding 150 K. Finally, PHONOPY code under the QHA was also used to calculate the temperature dependence of the isobaric heat capacity $C_p(T)$ of $CuFeS_2$, and the calculated values were in good agreement with experimental results for temperatures below 200 K, whereas the deviation between the two sets of results gradually increased at temperatures above 200 K owing to the lattice anharmonicity at higher temperatures.

SUPPLEMENTARY MATERIAL

See supplementary material for the polynomial fitting curves of the Helmholtz free energy per unit-cell volume for the six deformation modes with strain values (ζ) between ±3% in increments of 0.5% are provided.

ACKNOWLEDGMENTS

The authors would like to acknowledge and greatly appreciate financial support from VISTA, which is a basic research program in collaboration between the Norwegian Academy of Science and Letters and Equinor. The authors would also like to thank the Department of Mechanical and Industrial Engineering at the Norwegian University of Science and Technology (NTNU). The authors also acknowledge generous grants of high-performance computer time from both Vilje and UNINETT Sigma.

REFERENCES

[1] C. I. Pearce, R. A. D. Pattrick, D. J. Vaughan, C. M. B. Henderson, and G. Van der Laan, Geochimica et Cosmochimica Acta **70**(18), 4635–4642 (2006).
[2] R. C. Smith, Journal of Physics **36**, 89 (1975).
[3] P. Migliorato, B. Tell, J. L. Shay, and H. M. Kasper, Applied Physics Letters **24**(5), 227–228 (1974).
[4] Y. J. Zhao, P. Mahadevan, and A. Zunger, Applied Physics Letters **84**(19), 3753–3755 (2004).
[5] D. F. Marrón, A. Martí, and A. Luque, Thin Solid Films **517**(7), 2452–2454 (2009).
[6] L. Pauling and L. O. Brockway, Zeitschrift für Kristallographie **82**, 188 (1932).
[7] G. Donnay, L. M. Corliss, J. D. H. Donnay, N. Elliott, and J. M. Hastings, Physical Review **112**(6), 1917 (1958).
[8] J. C. Woolley, A. M. Lamarche, G. Lamarche, R. B. del Re, M. Quintero, F. Gonzalez-Jimenez, I. P. Swainson, and T. M. Holden, Journal of Magnetism and Magnetic Materials **164**(1-2), 154–162 (1996).
[9] T. Hamajima, T. Kambara, K. I. Gondaira, and T. Oguchi, Physical Review B **24**(6), 3349 (1981).
[10] C. H. L. Goodman and R. W. Douglas, Physica **20**(7-12), 1107–1109 (1954).
[11] B. I. Boltaks and N. N. Tarnovski, Zhurnal Tekhniceskoj Fiziki **25**, 402 (1955).
[12] I. G. Austin, C. H. L. Goodman, and A. E. Pengelly, Journal of the Electrochemical Society **103**(11), 609–610 (1956).
[13] C. I. Pearce, R. A. Pattrick, and D. J. Vaughan, Reviews in Mineralogy and Geochemistry **61**(1), 127–180 (2006).
[14] T. Teranishi, Journal of the Physical Society of Japan **16**(10), 1881–1887 (1961).
[15] T. E. Engin, A. V. Powell, and S. Hull, Journal of Solid State Chemistry **184**(8), 2272–2277 (2011).
[16] H. Takaki, K. Kobayashi, M. Shimono, N. Kobayashi, K. Hirose, N. Tsujii, and T. Mori, Applied Physics Letters **110**(7), 072107 (2017).
[17] H. Takaki, K. Kobayashi, M. Shimono, N. Kobayashi, K. Hirose, N. Tsujii, and T. Mori, Materials Today Physics **3**, 85–92 (2017).
[18] S. R. Hall and J. M. Stewart, Acta Crystallographica Section B: Structural Crystallography and Crystal Chemistry **29**(3), 579–585 (1973).
[19] T. Kratz and H. Fuess, Zeitschrift für Kristallographie **186**, 167–169 (1989).
[20] R. Khaledialidusti, A. K. Mishra, and A. Barnoush, The Journal of Chemical Physics **149**(22), 224702 (2018).
[21] J. Łażewski, H. Neumann, and K. Parlinski, Physical Review B **70**(19), 195206 (2004).

[22]M. Zhou, X. Gao, Y. Cheng, X. Chen, and L. Cai, Applied Physics A **118**(3), 1145–1152 (2015).
[23]S. Conejeros, P. Alemany, M. Llunell, I. D. P. Moreira, V. Sánchez, and J. Llanos, Inorganic Chemistry **54**(10), 4840–4849 (2015).
[24]R. Martínez-Casado, V. H. Y. Chen, G. Mallia, and N. M. Harrison, The Journal of Chemical Physics **144**(18), 184702 (2016).
[25]C. de Oliveira and H. A. Duarte, Applied Surface Science **257**, 1319–1324 (2010).
[26]S. L. Dudarev, G. A. Botton, S. Y. Savrasov, C. J. Humphreys, and A. P. Sutton, Physical Review B **57**(3), 1505 (1998).
[27]A. D. Becke, The Journal of Chemical Physics **98**(7), 5648–5652 (1993).
[28]C. Lee, W. Yang, and R. G. Parr, Physical Review B **37**(2), 785 (1988).
[29]G. Kresse and J. Hafner, Physical Review B **47**(1), 558 (1993).
[30]G. Kresse and J. Hafner, Physical Review B **49**(20), 14251 (1994).
[31]G. Kresse and J. Furthmüller, Computational Materials Science **6**(1), 15–50 (1996).
[32]G. Kresse and J. Furthmüller, Physical Review B **54**(16), 11169 (1996).
[33]J. P. Perdew and A. Zunger, Physical Review B **23**(10), 5048 (1981).
[34]K. Burke, J. P. Perdew, and M. Ernzerhof, Physical Review Letters **78**, 1396 (1997).
[35]J. Kitchin, Boston, Free Software Foundation (2008).
[36]A. H. Larsen, J. J. Mortensen, J. Blomqvist, I. E. Castelli, R. Christensen, M. Dułak, J. Friis, M. N. Groves, B. Hammer, C. Hargus, E. D. Hermes, P. C. Jennings, P. B. Jensen, J. Kermode, J. R. Kitchin, E. L. Kolsbjerg, J. Kubal, K. Kaasbjerg, S. Lysgaard, J. B. Maronsson, T. Maxson, T. Olsen, L. Pastewka, A. Peterson, C. Rostgaard, J. Schiøtz, O. Schütt, M. Strange, K. S. Thygesen, T. Vegge, L. Vilhelmsen, M. Walter, Z. Zeng, and K. W. Jacobsen, Journal of Physics: Condensed Matter **29**(27), 273002 (2017).
[37]K. Momma and F. Izumi, Journal of Applied Crystallography **44**(6), 1272–1276 (2011).
[38]X. Gonze and C. Lee, Physical Review B **55**(16), 10355 (1997).
[39]S. Baroni, S. De Gironcoli, A. Dal Corso, and P. Giannozzi, Reviews of Modern Physics **73**(2), 515 (2001).
[40]A. Togo, F. Oba, and I. Tanaka, Physical Review B **78**(13), 134106 (2008).
[41]A. Togo and I. Tanaka, Scripta Materialia **108**, 1–5 (2015).
[42]A. Togo, L. Chaput, I. Tanaka, and G. Hug, Physical Review B **81**(17), 174301 (2010).
[43]R. Edelbro, A. Sandstrom, and J. Paul, Applied Surface Science **206**, 300 (2003).
[44]F. D. Murnaghan, Proceedings of the National Academy of Sciences **30**(9), 244–247 (1944).
[45]F. Birch, Physical Review **71**, 809–824 (1947).
[46]T. Shao, B. Wen, R. Melnik, S. Yao, Y. Kawazoe, and Y. Tian, Journal of Applied Physics **111**(8), 083525 (2012).
[47]R. A. Robie, L. B. Wiggins, P. B. Barton, Jr., and B. S. Hemingway, The Journal of Chemical Thermodynamics **17**(5), 481–488 (1985).
[48]B. Wen, T. Shao, R. Melnik, Y. Kawazoe, and Y. Tian, Journal of Applied Physics **113**(10), 103501 (2013).
[49]N. N. Sirota and Zh. K. Zhalgasbekova, Doklady Akademii Nauk SSSR **321**, 513 (1991).
[50]P. Sisodia and M. P. Verma, Physica Status Solidi A **122**, 525 (1990).
[51]T. Tinoco, J. P. Itié, A. Polian, A. San Miguel, E. Moya, P. Grima, J. Gonzalez, and F. Gonzalez, Le Journal de Physique IV **4**(C9), C9–151 (1994).